Buckling analysis of multi-span non-uniform beams with functionally graded graphene-reinforced foams

Kang Gao [a,b], Huiyin Huang [a*], Zhiqiang Zou [a], Zhangming Wu [b], Hong Zhu [a**], Jie Yang [c]

[a] Key Laboratory of Concrete and Prestressed Concrete Structures of the Ministry of Education, School of Civil Engineering, Southeast University, Nanjing, China

[b] School of Engineering, Cardiff University, The Parade, Cardiff CF24 3AA, UK

[c] School of Engineering, RMIT University, PO Box 71, Bundoora, VIC 3083 Australia

Abstract

This paper conducts the buckling analysis of multi-span functionally graded (FG) beams reinforced by three-dimensional graphene foams (3D-GFs) restrained by elastic supports. The graphene foams are considered as graded variation in the thickness direction according to four different porosity distributions. The width and height of the non-uniform beams vary in the longitudinal direction in accordance with the power-law principle, and the multi-span beams consist of two types of optional beams. The governing equations of buckling behavior are derived based on the Timoshenko beam theory and the principle of virtual displacements, and solved by the discrete singular convolution (DSC) method. The purpose of this paper is to obtain the critical buckling load of FG 3D-GFs reinforced beams under the consideration of variable cross-section and multi-span beams with 2-4 spans. The effect of porosity coefficients, slenderness ratio, and spring constants on the buckling characteristic also are studied. The results suggest that the taper ratio of beams and the configuration of multi-span beams lead to remarkable changes in the critical buckling load of beams.

Keywords

Functionally graded beams, 3D graphene foams reinforcement; buckling analysis; multi-span beams; non-uniform section; elastic constrained; DSC method

*Corresponding author: huiyinhuang@seu.edu.cn
**Corresponding author: alice_zhuhong@seu.edu.cn

1. Introduction

Advanced structures made of functional gradient materials (FG materials) acquire customizable properties via spatial hierarchy [1], which have been widely applied in automotive, marine, aerospace, and civil engineering fields for their light-weight and high-strength performance, superior energy-absorption capability [2]. While metallic or ceramic-based FG materials have been widely employed in engineering structures, there is increasing attention on FG materials reinforced by nanomaterials, particularly graphene due to their exceptional mechanical strength and remarkable flexibility, offering new opportunities for innovative applications in various fields [3-5]. To expand the capabilities of FG graphene reinforced structures under buckling load, the utilization of three-dimensional graphene foams (3D-GFs) is being explored as a novel and effective reinforcement, which can achieve extensive supportability in large-scale applications by overcoming the agglomeration of two-dimensional (2D) graphene sheets [6, 7]. Therefore, FG structures reinforced by 3D-GFs (FG 3D-GFs), as one of the inventive developments in 3D porous network structures, have gained growing interest in the fields of biomedicine [8], electronics [9] and energy absorption [10] for their significant material properties and optimized function achieved through adjusting the 3D-GFs reinforcement patterns.

Beams are widely used in engineering industry, and the design and application of beams enable buildings, bridges, mechanical equipment, etc. to bear and distribute the loads [11-15]. In particular, beam structures are often subjected to axial compressive forces in engineering fields that can emerge in buckling phenomenon, which affects the stability and security of systems [16, 17]. Therefore, the buckling behavior of beams remains a critical factor in assessing the beams bearing capacity, and some researches about buckling analysis have been reported in the available kinds of literature. Thai [18] investigated the buckling of nanobeams by utilizing a nonlocal shear deformation beam theory. Vo and Thai [19] analyzed the buckling behavior of arbitrary lay-ups by the refined shear deformation theory. Based on different constraint conditions, Li et al. [20] explored the critical buckling load of Timoshenko beams, and further highlighted the intrinsic correlations in buckling loadings between Timoshenko beams and Euler-Bernoulli beams. Meanwhile, many studies focused on FG beams, Lanc et al. [21] exhibited the buckling characteristic of FG sandwich box beams using the Euler-Bernoulli beam theory, they also discussed the effect of FG box beams material properties obeying power-law relationship on the buckling response. Similarly, under the premise that beams material followed the power-law principle, Nguyen et al. [22] investigated the buckling performance of thin-walled FG open-section beams subjected to an axial force. Considering the effect of graphene nano-platelets (GPLs) reinforcement, Yang et al. [23] analyzed the buckling behavior of FG porous arch structures reinforced by GPLs under a stepwise applied load with rotationally restrained. Belarbi et al. [24] took FG carbon nanotubes reinforced beams as the research object and studied the buckling response of the beam experiencing diverse boundary conditions through the Hermite-Lagrangian finite element formulation to model the beams. However, the study about the buckling resistance of FG 3D-GFs reinforced beams is still lacking.

Multi-span beams are known for their enhanced flexibility and notable stretchability, which are applicable in engineering fields like aerospace, navigation, bridges, and water conservancy. In comparison to single-span beams, their unique characteristic made them idea for addressing complex engineering challenges [25-28]. Moreover, taking into consideration the buckling load, the prediction and control of the buckling behavior of multi-span beams require to be comprehensively and systematically studied. For instance, Xie [29] produced the impact of localization factors on the buckling response of multi-span continuous beams. Besides, Nikolić [17] analyzed the buckling characteristic of multi-span beams by applying the modified segmented rod method. In the meantime, Liu et al. [30] investigated the influence of parameters such as the number of spans and the length of each span on the thermal buckling of multi-span sandwich beams with lattice cores. Avetisyan et al. [31] explored the stability of finite length multi-span beams based on the Bloch-Floquet’s method. Based on bidirectional FG material, Heydari and Shariati [32] presented the buckling behavior of FG Euler-Bernoulli nano-beams and discussed the effect of various circumstances including non-uniform section, distribution of material and boundary conditions like the multi-span beams. Despite such outstanding performance of FG 3D-GFs reinforced beams, the research on multi-span reinforced beams’ stability behavior is still very limited.

Boundary conditions play a pivotal role in the investigation of FG 3D-GFs reinforced beams’ buckling behavior, as they can affect the stiffness of beams. However, achieving the idealized classical boundary conditions proves challenging for the uncontrollable support force, sliding and jumping friction of the supports [33]. These unpredictable conditions introduce new complexities to research, requiring approaches to accurately account for realistic boundary conditions of systems. Therefore, Butcher et al. [34] recommended using springs to represent the actual boundary conditions, referred to as elastic restraint. Li et al. [35] analyzed the stability of beams under simply-simply support, clamp-simply support, and elastic restraint at both boundaries by using the DSC method. Tam et al.[36] constrained the FG graphene nano-platelets reinforced beams with various stiffness elastic boundary conditions, and applied the finite element method to study the beam nonlinear static behavior. Besides, Raffo et al. [37] applied elastic restraints to intermediate locations of beam to analyze the mechanical behavior of beam. Zhang et al. [38] utilized the Euler-Bernoulli beam theory to explore the buckling response of a spring-supported double beam in the face of an axial force. Ariaei et al. [39] studied the dynamic behavior of multi-span beams connected by elastic springs to adjacent span beams. Ghorbanpour-Arani et al. [40] studied the elastic effect of surrounded medium on the dynamic behavior of FG magnetostrictive sandwich nanobeams.

Furthermore, the current body of research on buckling analysis predominantly focuses on uniform section beams, there is a dearth of research on the buckling analysis conducted by non-uniform sectional beams as the subject of investigation, while the non-uniform beams hold great potential in meeting the unique functional demands in construction, robotics, aviation, and beyond [41-43]. Therefore, it becomes imperative to delve into the buckling analysis of non-uniform beams to ensure the stability of these applications. Li [44] investigated the buckling characteristic of multi-step non-uniform beams with the elastic restraint located in the beams' end and intermediate points. Subsequently, Li [45] went on to study the buckling behavior of non-uniform beams with an arbitrary number of cracks. Rajasekaran and Khaniki [46] conducted the buckling behavior of small-scale tapered beams with non-uniform cross section according to Hamilton's principle and gained the governing equations through the finite element method. For FG beams, Chen et al. [47] changed the beams section and solved the buckling problem of beams under compression stress wave, combining the differential element method and the principle of energy conservation. Considering the geometric defect including sine, global and local three modes, Lin et al. [48] obtained the critical buckling load of FG carbon nanotubes reinforced beams.

This paper conducts the buckling responses of non-uniform FG 3D-GFs reinforced multi-span beams under elastic boundary conditions. The 3D graphene foams reinforcements are considered to be a gradient distribution across the thickness of beams and the material properties of beams are determined according to the four porosity distribution patterns. Followed by the power-law principle, two types of non-uniform single-span beams have been developed, and each cross section varies along the beams' length. Furthermore, various form of multi-span beams are achieved by combining these two types of beams in diverse ways. The governing equations of buckling are derived from the Timoshenko beam theory and the virtual displacements principle, and then solved numerically based on the DSC algorithm. The effects of different system parameters and the configuration of multi-span beams are discussed in detail, which aims to enhance the structural stability and buckling performance of these beams.

2. 3D-GFs reinforced beams with porosities

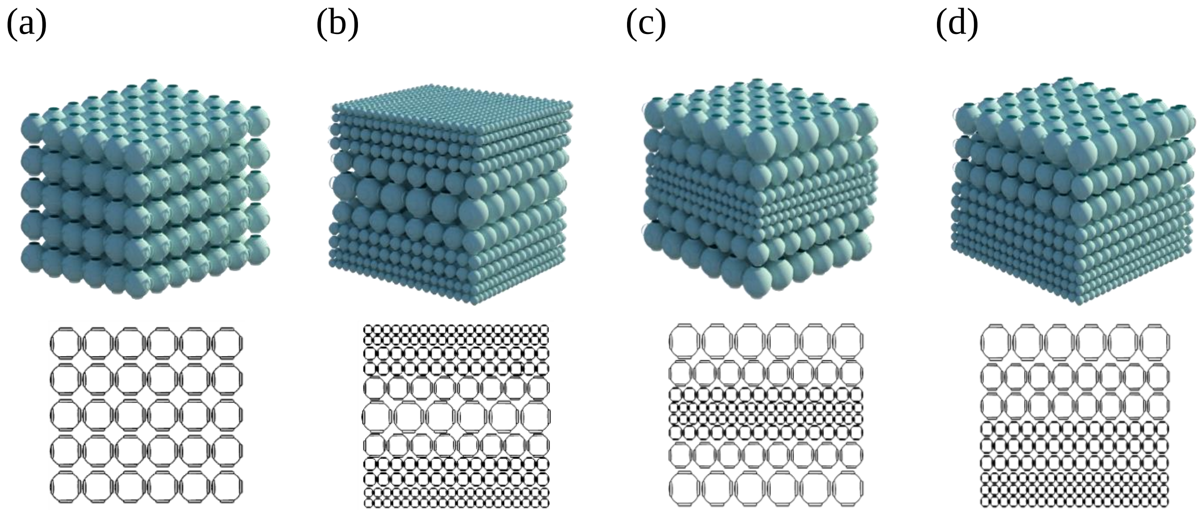

Fig. 1 The schematic diagrams of four patterns porosity distribution 3D-GFs reinforced beams. (a) Pattern 1; (b) Pattern 2; (c) Pattern 3; (d) Pattern 4.

3D graphene foams are distributed in different ways to form four patterns of FG beams, and their material properties gradients are distributed along beams thickness according to 3D-GFs reinforcement variation. The schematic diagrams of the four pattern beams are exhibited in Fig. 1.

Eq. (1) serves to characterize the mechanical properties, the elastic modulus E, shear modulus G, and material density ρ of Pattern 1 to Pattern 4 beams, and it is assumed that the Poisson's ratio (v) remains constant throughout the material [49] for simplifying calculation and accurate predicting the buckling behavior of beams.

$$\begin{cases} E(z) = E_{\max}[1 - N_0\xi(z)] \\ G(z) = E(z)/[2(1+\nu)] \\ \rho(z) = \rho_{\max}[1 - N_m\xi(z)] \end{cases} \tag{1}$$

where $\xi(z)$ are

$$\xi(z) = \begin{cases} \xi_0 & \text{Pattern 1} \\ \cos(\pi z/h) & \text{Pattern 2} \\ 1-\cos(\pi z/h) & \text{Pattern 3} \\ \cos(\pi z/2h + \pi/4) & \text{Pattern 4} \end{cases} \tag{2}$$

The $E_{\max}$, $E_{\min}$, $G_{\max}$, and $G_{\min}$ can be utilized to derive the porosity coefficient $N_0 = 1 - E_{\min}/E_{\max} = 1 - G_{\min}/G_{\max}$ $(0 < N_0 < 1)$ and the porosity coefficient of mass density $N_m = 1 - \rho_{\min}/\rho_{\max}$ $(0 < N_m < 1)$. Based on the relationship between material density ρ and elastic modulus E given by Eq. (3), the correlation between N_0 and N_m can be determined expressed as Eq. (4).

$$\frac{E_{\max}}{E_{\min}} = \left(\frac{\rho_{\max}}{\rho_{\min}}\right)^2 \tag{3}$$

$$N_m = 1 - \sqrt{1 - N_0} \tag{4}$$

Moreover, beams with different porosity distributions possess identical total mass, therefore, the mass density porosity coefficient of uniform porosity distribution beams (N_m^*) can be achieved according to the equivalence of total mass among the beams expressed by N_0 and exhibited in Eq. (5)

$$N_m^* = \frac{1 - \sqrt{1 - N_0\xi_0}}{\xi_0}\left(0 < N_m^* < 1\right); \quad \xi_0 = \frac{1 - [1 - 2N_m/\pi]^2}{N_0} \tag{5}$$

As shown in Fig. 1 and Eq. (1), Pattern 1 beam has homogeneous foam distribution and consistent material characteristics. Pattern 2 beam shows a symmetric porosity profile confined to the middle region of beam thickness, whose foams density are highest at the top and the bottom surfaces, and steadily decrease during the thickness axis towards the lowest density at the center plane. Specifically, the outer surfaces of the beam have the $E_{\max}$, $G_{\max}$ and $\rho_{\max}$, while the mid-plane exhibits $E_{\min}$, $G_{\min}$ and $\rho_{\min}$. On the other hand, the material properties of Pattern 3 beam are opposite to the distribution of Pattern 2 beam. Moreover, Pattern 4 beam exhibits an asymmetrical variation, whose maximum material properties gradually decreases from the lower surface to obtain the minimum properties.

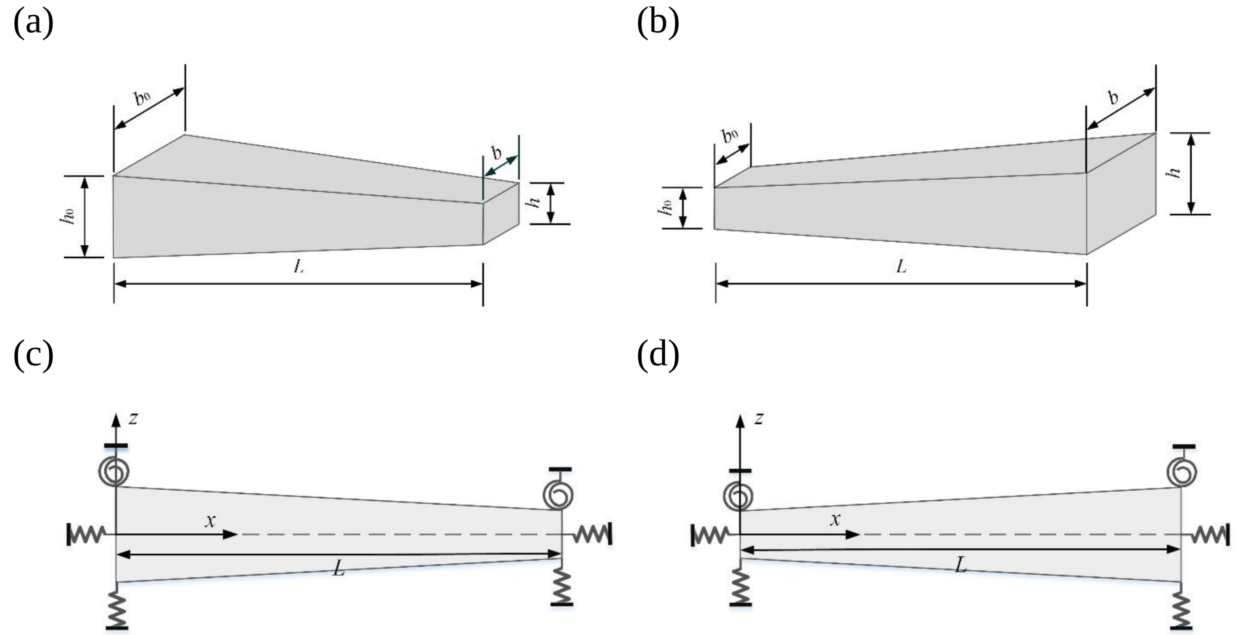

Fig. 2 Two basal non-uniform sectional single-span beams. (a) The geometry of T1S1 beam; (b) The geometry of T2S1 beam; (c) The Cartesian coordinate system of T1S1 beam; (d) The Cartesian coordinate system of T2S1 beam.

In addition, it is worth noting that two types of optional single-span FG beams reinforced by 3D-GFs are discussed in this paper, namely Type1 (T1) and Type2 (T2) beams, which are simplified as T1S1 and T2S1 beams by combining the number of beam span. S indicates the number of spans, and the designations S2-S4 are assigned to represent two-span beams, three-span beams, and four-span beams. Fig. 2 presents these two basal non-uniform sectional single-span beams varying along the length direction under elastic support (E-E), where the beams are supported by axial, translational, and rotational springs at both ends.

As seen in Fig. 2, T1S1 beam is represented by a gradually decreasing section from the beginning to the end. Conversely, T2S1 beam is obtained by rotating the T1S1 beam through 180 degrees. Therefore, the initial section dimensions value of T1S1 beam are equivalent to the tail end dimensions value of T2S1 beam, which implies h_0 (T1)=h (T2), b_0 (T1)=b (T2). Their cross-sectional height $h(x)$ and width $b(x)$ vary horizontally based on the power-law regulation, shown as Eq. (6) for T1S1 beam and Eq. (7) for T2S1 beam.

$$\begin{cases} h(x) = h_0 \left(1 - \alpha \dfrac{x}{L}\right)^m \\ b(x) = b_0 \left(1 - \beta \dfrac{x}{L}\right)^n \end{cases} \tag{6}$$

$$\begin{cases} h(x) = h \left(1 - \alpha \left(1 - \dfrac{x}{L}\right)\right)^m \\ b(x) = b \left(1 - \beta \left(1 - \dfrac{x}{L}\right)\right)^n \end{cases} \tag{7}$$

where b_0 (T1S1)=b (T2S1)=1, L=1, the coefficient of height variation α and width variation β can be described by Eq. (8), and can be all classified as taper ratio (τ) for convenient reference, and the default is $\tau = \alpha = \beta$.

$$\begin{cases} \alpha = 1 - \dfrac{h}{h_0}(\text{T1S1}) = 1 - \dfrac{h_0}{h}(\text{T2S1}) \qquad (0 \le \alpha \le 1) \\ \beta = 1 - \dfrac{b}{b_0}(\text{T1S1}) = 1 - \dfrac{b_0}{b}(\text{T2S1}) \qquad (0 \le \beta \le 1) \end{cases} \tag{8}$$

The beam is considered to have a uniform cross section when $\tau = \alpha = \beta = 0$, and the linear profile represented by m=1 and n=1 is adopted in this paper.

Moreover, this paper explores the buckling properties of various models multi-span beams based on the diverse combinations of Type1 and Tyep2 beams. Therefore, the cross-sectional dimensions of each span beam under multi-span beams still follow Eq. (6) and Eq. (7). The different model of non-uniform section multi-span beams for Pattern 3 porosity distribution are demonstrated in Fig. 3. Among them, T1 and T2 refer to the use of Type1 and Type2 beams, respectively, as the first span beam in the multi-span beams.

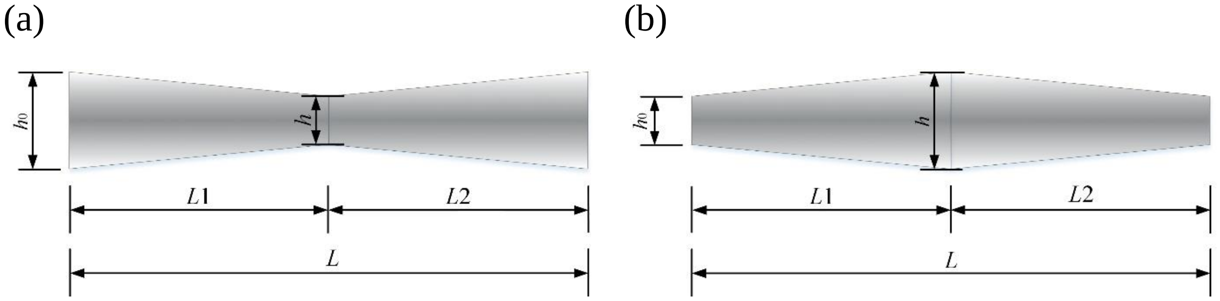

(c) (d)

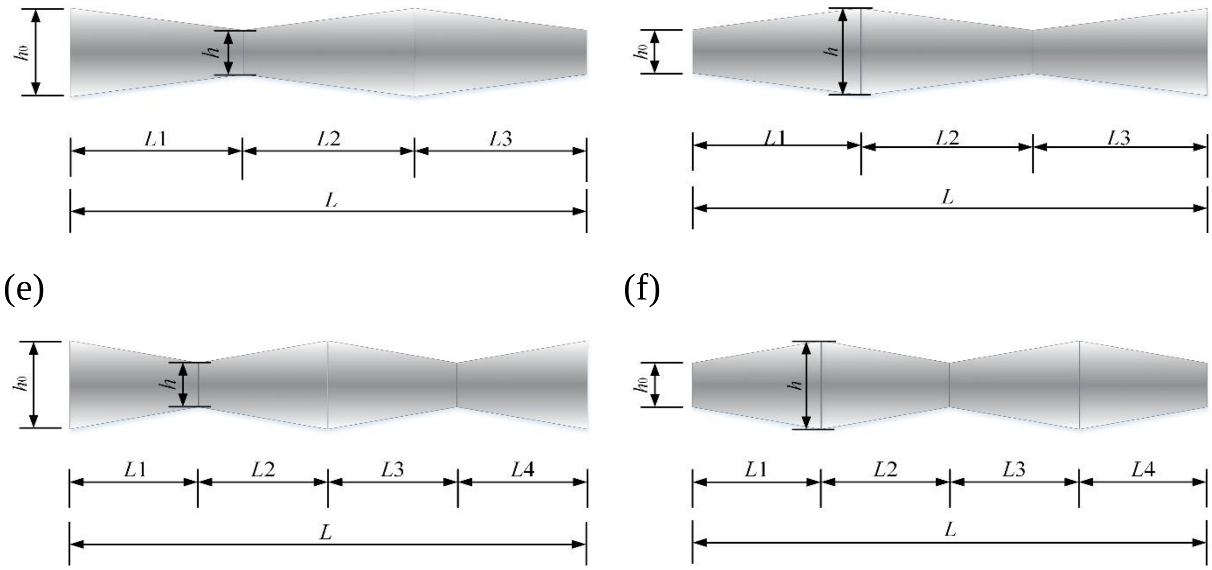

Fig. 3 Different models of non-uniform section multi-span beams for Pattern 3 porosity distribution. (a) T1S2 beam; (b) T2S2 beam; (c) T1S3 beam; (d) T2S3 beam; (e) T1S4 beam; (f) T2S4 beam.

3. 3D-GFs reinforced beams buckling analysis

The resistance buckling ability of beams is a vital issue in engineering applications, therefore, the buckling analysis of FG 3D-GFs reinforced beams is required. Firstly, the buckling governing equations are derived by using the principle of virtual displacement combined with the Timoshenko beam theory, and then the derivative equations of the displacements are solved by the DSC method to obtain the final governing equation.

3.1. Governing equation

The principle of virtual displacements is employed to derive the governing equations of beams in this paper, and the following equation is shown as

$$\delta U - \delta W = 0 \tag{9}$$

where U and W represent the strain energy and the work done by the external force N_{x0} on the elastomer, respectively. They are solved by the Timoshenko beam theory in conjunction with displacement fields along the beam axes x and z which are given by the following expression.

$$u_x\left(x,z\right) = u_0(x) + z\varphi_x(x) \tag{10}$$

$$u_z\left(x,z\right) = w_0(x) \tag{11}$$

where $u_0(x)$ and $w_0(x)$ are the longitudinal and transverse displacements along the x-axis and

z-axis at the mid-plane (z=0) of the beam respectively, $\varphi_x(x)$ is the mid-plane rotation of transverse normal about the x-axis. The geometric and physical equations of the beam are

$$\varepsilon_{xx} = \frac{\partial u_0}{\partial x} + z\frac{\partial \varphi_x}{\partial x}, \quad \gamma_{xz} = \frac{\partial w_0}{\partial x} + \varphi_x \tag{12}$$

$$\sigma_{xx} = \frac{E(z)}{1-v^2}\varepsilon_{xx}, \quad \tau_{xz} = G(z)\gamma_{xz} = \frac{E(z)}{2(1+v)}\gamma_{xz} \tag{13}$$

Substituting Eq. (12) into Eq. (13), the integral obtains the axial force (F) and bending moment (M) as

$$\begin{bmatrix} F \\ M \end{bmatrix} = \begin{bmatrix} A_{11} & B_{11} \\ B_{11} & D_{11} \end{bmatrix} \begin{bmatrix} \frac{\partial u_0}{\partial x} \\ \frac{\partial \varphi_x}{\partial x} \end{bmatrix} \tag{14}$$

And the shear force (V) is expressed as

$$V = \int_A \sigma_{xz} dA = \kappa_s A_{55}\gamma_{xz} \tag{15}$$

where $[F, M] = \int_A \sigma_{xx}[1, z]dA$, κ_s is the shear correction factor. A_{11}, A_{55}, B_{11}, D_{11} are the stiffness components obtained according to the differential principle, and they are shown as [50]

$$[A_{11}, B_{11}, D_{11}] = \int_A \frac{E(z)}{1-v^2}[1, z, z^2]dA = b\int_{-h/2}^{h/2} \frac{E(z)}{1-v^2}[1, z, z^2]dz \tag{16}$$

$$A_{55} = \int_A \frac{E(z)}{2(1+v)}dA = b\int_{-h/2}^{h/2} \frac{E(z)}{2(1+v)}dz \tag{17}$$

Therefore, the first-order variation of the strain energy of the beam is defined as

$$\begin{aligned} \delta U &= \int_V (\sigma_{ij}\delta\varepsilon_{ij} + \sigma_{ij}\delta\gamma_{ij})dV = \int_V (\sigma_{xx}\delta\varepsilon_{xx} + \sigma_{xz}\delta\gamma_{xz})dV \\ &= \int_0^L (\frac{\partial F}{\partial x}\delta u_0 - \frac{\partial M}{\partial x}\delta\varphi_x + \frac{\partial V}{\partial x}\delta w_0 + V\delta\varphi_x)dx \end{aligned} \tag{18}$$

Besides, the first-order variation of the work done by N_{x0} of the beam is

$$\delta W = \int_0^L N_{x0}\frac{\partial^2 w_0}{\partial x^2}\delta w_0 dx \tag{19}$$

Substituting Eq. (18) and Eq. (19) into Eq. (9) gives

$$\int_0^L \left[(\frac{\partial F}{\partial x})\delta u_0 + (\frac{\partial V}{\partial x} - N_{x0}\frac{\partial^2 w_0}{\partial x^2})\delta w_0 + (-\frac{\partial M}{\partial x} + V)\delta\varphi_x \right] dx = 0 \tag{20}$$

Since δu_0, δw_0 and $\delta \varphi_x$ cannot be zero, the motion governing equations of the beam deduced by the virtual displacements principle can be expressed as

$$\begin{cases} \dfrac{\partial F}{\partial x} = 0 \\ \dfrac{\partial V}{\partial x} - N_{x0} \dfrac{\partial^2 w_0}{\partial x^2} = 0 \\ -\dfrac{\partial M}{\partial x} + V = 0 \end{cases} \tag{21}$$

By substituting Eq. (14) and Eq. (15) into Eq. (21), the governing equations of motion are rewritten as

$$\begin{cases} A_{11} \dfrac{\partial^2 u_0}{\partial x^2} + B_{11} \dfrac{\partial^2 \varphi_x}{\partial x^2} = 0 \\ \kappa_s A_{55} \left(\dfrac{\partial^2 w_0}{\partial x^2} + \dfrac{\partial \varphi_x}{\partial x} \right) = N_{x0} \dfrac{\partial^2 w_0}{\partial x^2} \\ B_{11} \dfrac{\partial^2 u_0}{\partial x^2} + D_{11} \dfrac{\partial^2 \varphi_x}{\partial x^2} - \kappa_s A_{55} \left(\dfrac{\partial w_0}{\partial x} + \varphi_x \right) = 0 \end{cases} \tag{22}$$

3.2. *Discrete singular convolution (DSC) method*

This paper utilized the discrete singular convolution (DSC) method as a computational technique to effectively solve the governing equations of buckling behavior for FG 3D-GFs reinforced beams, which was proposed by Wei in 1999 [51]. The DSC method allows the differential equations to be solved as a set of algebraic equations, where the values of functions at the nodes are achieved by discretising the *n*th-order derivatives of the formula using a discrete singular convolution [52]. The utilization of the DSC method was intended to address the computational implementation of singular convolutions encompassing Hilbert, Abel, and delta types, which can be extensively applied in practical science and engineering areas [53]. Particularly, the DSC method seamlessly combines the precision of global integration methods with the adaptability of local methods, enabling effective handling of intricate geometries and boundary conditions by correct choosing the parameters of the DSC kernel [53-57]. In DSC, the derivative of the function can be calculated as [58, 59]

$$f^{(n)}(x) \approx \sum_{k=-M}^{M} \delta_{\sigma,\Delta}^{(n)}(x - x_k) f(x_k) \qquad (n\text{=0, 1, 2, …}) \tag{23}$$

where x_k are a set of equally spaced grid points that surround the point x. $2M+1$ is referred to as the calculation bandwidth, where N-1 is the maximum possible value of M, and N represents the total number of calculation nodes in each span beam exhibited in Eq. (24).

$$N = Nn \times Ns - (Ns - 1) \tag{24}$$

where Ns is the number of segments where the beam is divided into, Nn is the calculation nodes in each segment.

Besides, the nth derivative of the delta kernel of Dirichlet type, the Regularized Shannon's kernel (RSK), and the discretization parameter $r = \sigma/\Delta$ [59] are obtained in Appendix A.

According to the governing equations, the superscript n in Eq. (23) take the values of 1 and 2, so that the function $f(x)$ of DSC method are denoted in Appendix B.

To remove the fictitious points located beyond the physical domain, the boundary conditions processing technique, known as Taylor series expansion [60, 61], are imposed in this paper. In regard to [62], the Taylor series expansion for $f(x)$ and $f(-x)$ at the point of x_0=0 are as

$$f(x) = f(0) + f^{(1)}(0)x + \frac{1}{2!}f^{(2)}(0)x^2 + \frac{1}{3!}f^{(3)}(0)x^3 + \frac{1}{4!}f^{(4)}(0)x^4 + \frac{1}{5!}f^{(5)}(0)x^5 + \ldots \tag{25}$$

$$f(-x) = f(0) - f^{(1)}(0)x + \frac{1}{2!}f^{(2)}(0)x^2 - \frac{1}{3!}f^{(3)}(0)x^3 + \frac{1}{4!}f^{(4)}(0)x^4 - \frac{1}{5!}f^{(5)}(0)x^5 + \ldots \tag{26}$$

In the case of satisfying the computation precision, the sum of Eq. (25) and Eq. (26) can be simplified as

$$f(-x) = -f(x) + 2f(0) + f^{(2)}(0)x^2 \tag{27}$$

Likewise, $f(x)$ and $f(-x)$ at the point of x_{N-1}=L can be rewritten as

$$f(-x) = -f(x) + 2f(L) + f^{(2)}(L)(x-L)^2 \tag{28}$$

By means of Eq. (27) and Eq. (28), the fictitious points outside the beam are eliminated. The function $f(x)$ of 1st- and 2nd-order derivatives based on Taylor series expansion can be demonstrated in Appendix B. Therefore, the governing equations of motion can also be procured in Appendix B.

4. Assembly and solution methodologies

In term of the multi-span beams considered in this paper, each span beam is defined as an element within the multi-span beams, so that the number of beam elements depend on the number of beam spans. After utilizing the boundary conditions and governing equations, the dimension of the stiffness matrix for each element is (3N+6)×(3N+6). Moreover, the continuity problem of each single-span beam is critical to be taken into account. The following is an example of the two-span beam, where each span beam has N calculation nodes from 0 to N-1, and the node labeled as N-1 in the first span beam serves as the common node connecting the two individual single-span beams. The displacements of node N-1 should be continuous and equal for the ends of two-span beams, i.e. $\bar{u}_{N-1} = [\bar{u}_{N-1}]_{①}^{-} = [\bar{u}_0]_{②}^{+}$, $\bar{w}_{N-1} = [\bar{w}_{N-1}]_{①}^{-} = [\bar{w}_0]_{②}^{+}$ and $\bar{\varphi}_{N-1} = [\bar{\varphi}_{N-1}]_{①}^{-} = [\bar{\varphi}_0]_{②}^{+}$. By using springs with various stiffness to represent the elastic support, the boundary force equilibrium equations of the multi-span beams referred to [63] are as follows in Appendix C.

Another point to consider the multi-span beams connection problem is that there are nine unknown degrees of freedom at the common node, $\bar{u}_{N-1}$, $\left[\bar{u}_{N-1}^{(2)}\right]_{①}^{-}$, $\left[\bar{u}_0^{(2)}\right]_{②}^{+}$, $\bar{w}_{N-1}$, $\left[\bar{w}_{N-1}^{(2)}\right]_{①}^{-}$, $\left[\bar{w}_0^{(2)}\right]_{②}^{+}$, $\bar{\varphi}_{N-1}$, $\left[\bar{\varphi}_{N-1}^{(2)}\right]_{①}^{-}$, $\left[\bar{\varphi}_0^{(2)}\right]_{②}^{+}$, respectively. Therefore, nine formulas are required and shown as follow in Appendix C.

After combining the governing equations Eq. (22) with boundary conditions, the buckling equations of beams can be presented as the partitioned matrix shown below

$$\left[[\mathbf{K}] - P[\mathbf{V}]\right]\{\mathbf{d}\} = 0 \tag{29}$$

where $[\mathbf{K}]$ is the element stiffness matrix, $[\mathbf{V}]$ is the geometric stiffness matrix associated with the buckling load, and $\{\mathbf{d}\}$ is the different displacement components. They are given in Appendix D.

After implementation of $\{d_b\}$, Eq. (29) can be rewritten in a matrix form as

$$\left[\left[\tilde{\mathbf{K}}\right] - P\left[\tilde{\mathbf{V}}\right]\right]\{d_a\} = 0 \tag{30}$$

where $\left[\tilde{\mathbf{K}}\right]$ and $\left[\tilde{\mathbf{V}}\right]$ are given in Appendix D.

It is clear that the minimum eigenvalue calculated from Eq. (30) can receive the critical buckling load P.

5. Numerical analysis

A comprehensive parametric investigation is carried out to analyze the buckling behavior of FG 3D-GFs reinforced beams in this section. Various system parameters and the configuration of multi-span beams are considered in the subsequent portion. Besides, since T1S1 beams and T2S1 beams have the same structural shape and exhibit an identically mechanical response, the parametric analysis of single-span beams is conducted by using T1S1 beams as the primary target of research. 3D-GFs reinforcement material properties are v=1/3, $E_{\max} = 1020\,\text{GPa}$ and $\rho_{\max} = 2300\,\text{kg/m}^3$ [64]. For simplicity, the dimensionless critical buckling load and the dimensionless spring constant factors are introduced in Appendix E.

5.1.Convergence and validation

The total number of calculation nodes N controls the manufacturing cost and time consumption, which consists of the number of segments (Ns) and the calculation nodes in each segment (Nn). Therefore, in order to produce sufficiently accurate results at the lowest cost, it is necessary to determine the optimal Ns and Nn. The convergence study of Ns initiates firstly in Table. 1 and Table. 2 for T1S1 and T2S1 beams with Pattern 1 to Pattern 4 porosity distributions under the premise that Nn is equal to 100, which corresponds to a sufficient number of numerical nodes distributed appropriately within each beam segment. The boundary conditions of beams are E-E constraints, where the dimensionless spring constant factors are $\gamma_{LA} = \gamma_{RA} = 10^8$, $\gamma_{LT} = \gamma_{LR} = \gamma_{RT} = \gamma_{RR} = 10^2$. Table. 1 and Table. 2 convey that Ns=20 is the best choice, as the relative difference between its consequences and the results obtained by Ns=36 is less than 3%. After determining Ns=20, the convergence study of Nn for T1S1 and T2S1 beams are performed as shown in Fig. 4 and Fig. 5, where the dimensionless critical buckling load exhibit a steady trend when Nn=50 for four patterns porosity distribution. Therefore, for the subsequent analysis, a value of Nn=50 is employed. According to the dimensionless critical buckling load received from the convergence study, it is evident that the T1S1 and T2S1 beams indeed possess identical mechanical properties.

Table. 1 Convergence study of Ns for T1S1 ($\times 10^{-3}$). (L/h_0=10, $\tau = 0.5$, N_0=0.5)

Ns	Pattern 1	Pattern 2	Pattern 3	Pattern 4
2	4.573	5.510	4.734	4.667
6	4.832	5.809	5.011	4.932
10	4.760	5.724	4.936	4.858
15	4.740	5.708	4.921	4.835

20	4.757	5.690	4.909	4.974
25	4.757	5.674	4.915	4.827
30	4.792	5.718	4.905	5.419
36	4.731	5.690	4.929	4.834

Table. 2 Convergence study of *Ns* for T2S1 ($\times10^{-3}$). (L/h =10, $\tau = 0.5$, N_0=0.5)

Ns	Pattern 1	Pattern 2	Pattern 3	Pattern 4
2	4.573	5.510	4.734	4.667
6	4.832	5.809	5.012	4.932
10	4.760	5.724	4.936	4.859
15	4.740	5.701	4.916	4.834
20	4.736	5.693	4.908	4.828
25	5.129	5.702	4.907	4.825
30	4.727	5.697	4.913	5.276
36	4.740	5.683	4.937	4.825

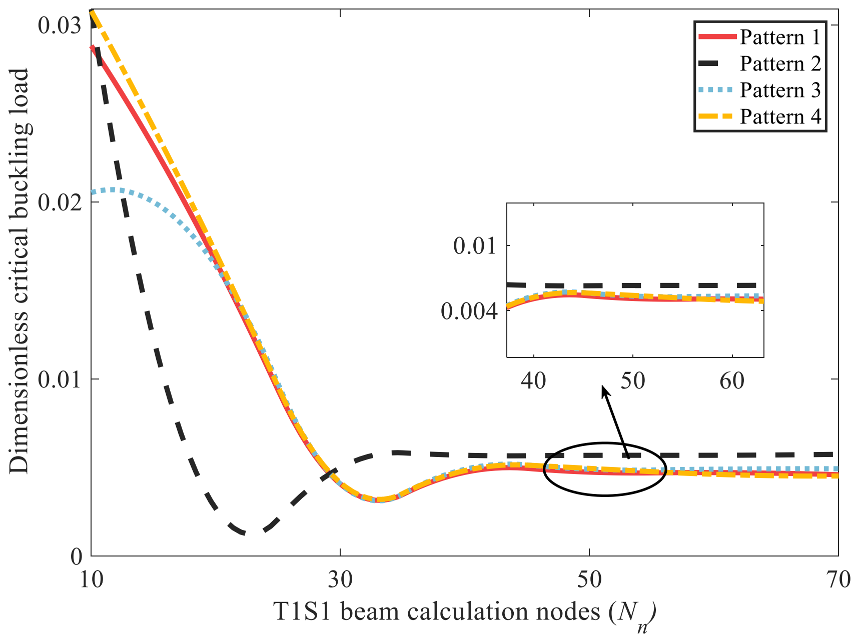

Fig. 4 Convergence study for T1S1 beams with varying calculation nodes. (L/h_0=10, $\tau = 0.5$, N_0=0.5)

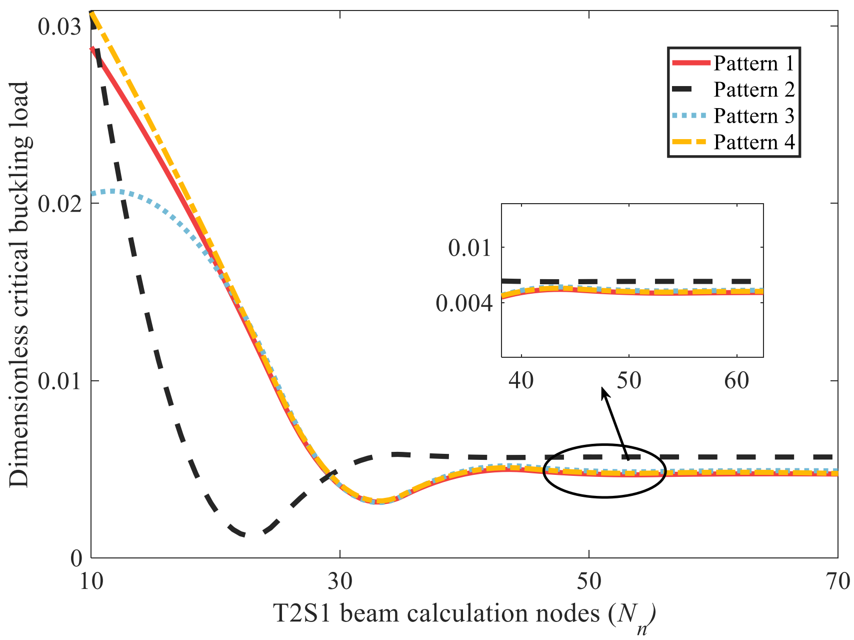

Fig. 5 Convergence study for T2S1 beams with varying calculation nodes. (L/h=10, $\tau = 0.5$, N_0=0.5)

The accuracy analysis of the present study is exhibited in Table. 3 by comparing the results given by Kitipornchai et al [65], where FG beams were calculated as multi-layered beams, and *n* represents the number of layers. To conform with the prerequisites in the study by Kitipornchai and his colleagues, the pure metal foam material properties were set to $E_{\max} = 130\,\mathrm{GPa}$, $\rho_{\max} = 8960\,\mathrm{kg/m^3}$, and the slenderness ratio L/h was 20. Besides, the comparison is shown in Table. 4 by the result given by Sayyad et al. [66]. The material properties of FG nanobeam were based on the power-law principle, and the dimensionless critical buckling load was expressed as $P_{cr} = 12L^2 N_{x0} / E_m h^3$, where the slenderness ratio L/h was 10. Moreover, Table. 5 demonstrates the validation of the present results with the data of Thai et al.[67] discussed. As can be observed, there are good agreement between our study and the published results under different conditions. Hence, the numerical model adopted in this paper is considered accurate.

Table. 3 Validation of the dimensionless critical buckling load of FG beams for Pattern 2 porosity distribution under clamp-clamp boundary condition ($\times 10^{-3}$).

Source	*n*	N_0			
		0	0.2	0.4	0.6

present	/	7.986	7.395	6.801	6.204
[65]	14	7.946	7.316	6.693	6.076
	10,000	7.986	7.362	6.745	6.135
Error (%)	/	0.000	0.446	0.823	1.112

Table. 4 Validation of the dimensionless critical buckling load of FG nanobeams for power-law principle distribution under simple support.

Source	*k*				
	0	0.5	1	5	10
present	52.162	33.916	26.113	17.163	15.561
[66]	52.240	33.968	26.142	17.077	15.498
Error (%)	0.149	0.154	0.109	0.505	0.405

Table. 5 Validation of the dimensionless critical buckling load of homogeneous beam under simple support.

Source	*L/h*			
	5	10	20	100
present	8.8328	9.5956	9.8075	9.8808
[67]	8.9533	9.6231	9.8068	9.8671
Error (%)	1.3460	0.2857	0.0074	0.1391

5.2. Buckling analysis of FG 3D-GFs reinforced beams

In this subsection, the effects of porosity coefficients, slenderness ratio, taper ratio, dimensionless spring constants, and multi-span beams under different boundary conditions on dimensionless critical buckling loads are discussed.

5.2.1 The influence of porosity coefficients

Fig. 6 presents the dimensionless critical buckling load of T1S1 beams variation curve with porosity coefficients (N_0) for three taper ratio under elastic restraint. As expected, an increase in porosity coefficients leads to a decrease in the dimensionless critical buckling load, regardless of the porosity distribution and the taper ratio. This phenomenon demonstrates that the internal porosity of beam is related to the beam stiffness, with larger beam porosity resulting in smaller beam stiffness. However, compared with other porosity distributions, the impact of the porosity coefficients on the stiffness of the Pattern 1 beam and Pattern 4 beam is more significant, as evidenced by the reduction magnitude in the dimensionless critical buckling load.

5.2.2 The influence of slenderness ratio

The influence of the slenderness ratio on the buckling performance of T1S1 beams with three taper ratio under elastic constraint are discussed in Fig. 7. Since the beam section in this paper is variable, the slenderness ratio is set as L/h_0 for T1S1 beams. As shown, the increase in slenderness ratio results in a reduction of the beams dimensionless critical buckling load for four patterns porosity distribution. Particularly for slenderness ratio ranging from 5 to 15, the dimensionless critical buckling load of beams decline the most, while it decreases moderately for slenderness ratio between 15 and 25. Finally, when the slenderness ratio is 25 to 35, the dimensionless critical buckling load gradually tends to stabilize.

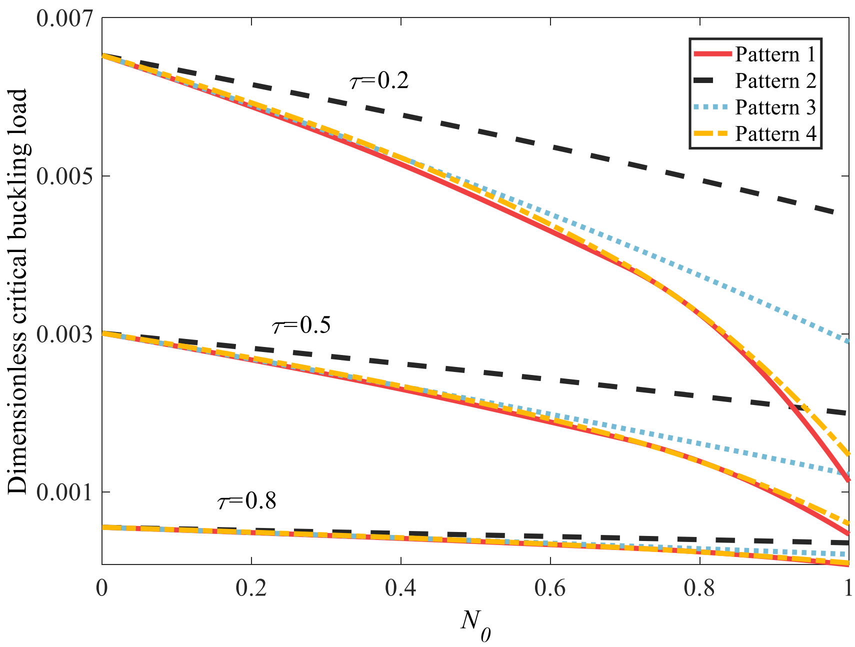

Fig. 6 Dimensionless critical buckling load of T1S1 beams with varying N_0. (L/h_0=15)

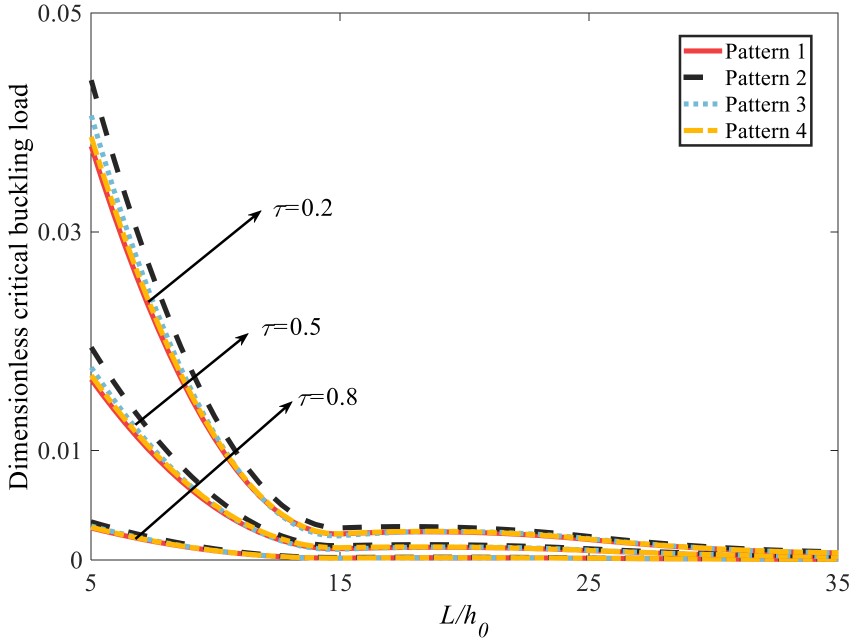

Fig. 7 Dimensionless critical buckling load of T1S1 beams with varying L/h_0. (N_0=0.5)

5.2.3 The influence of the taper ratio

With regard to the beam model analyzed in this paper incorporating the non-uniform section factor, it is necessary to explore the influence of taper ratio on the beam buckling load. Fig. 8 depicts the dimensionless critical buckling load of T1S1 beams with the varying α and β under the elastic boundary conditions. For these four patterns porosity distribution, the beam dimensionless critical buckling load decreases as α and β increase. However, when α =0 and β is increasing, the effect on the beam stiffness is smaller than that when β =0 and α is increasing, which implies that the impact of height variation is much more significant than that of width variation on the beam buckling resistance. Furthermore, combined with the enlarged picture on the right, it can be seen that as the taper ratio increases, Pattern 2 beam obtains the maximum dimensionless critical buckling load, while the minimum dimensionless critical buckling load occurs at Pattern 1 beam. As for Pattern 3 and 4 beams exhibit similar critical buckling load which fall in the middle position.

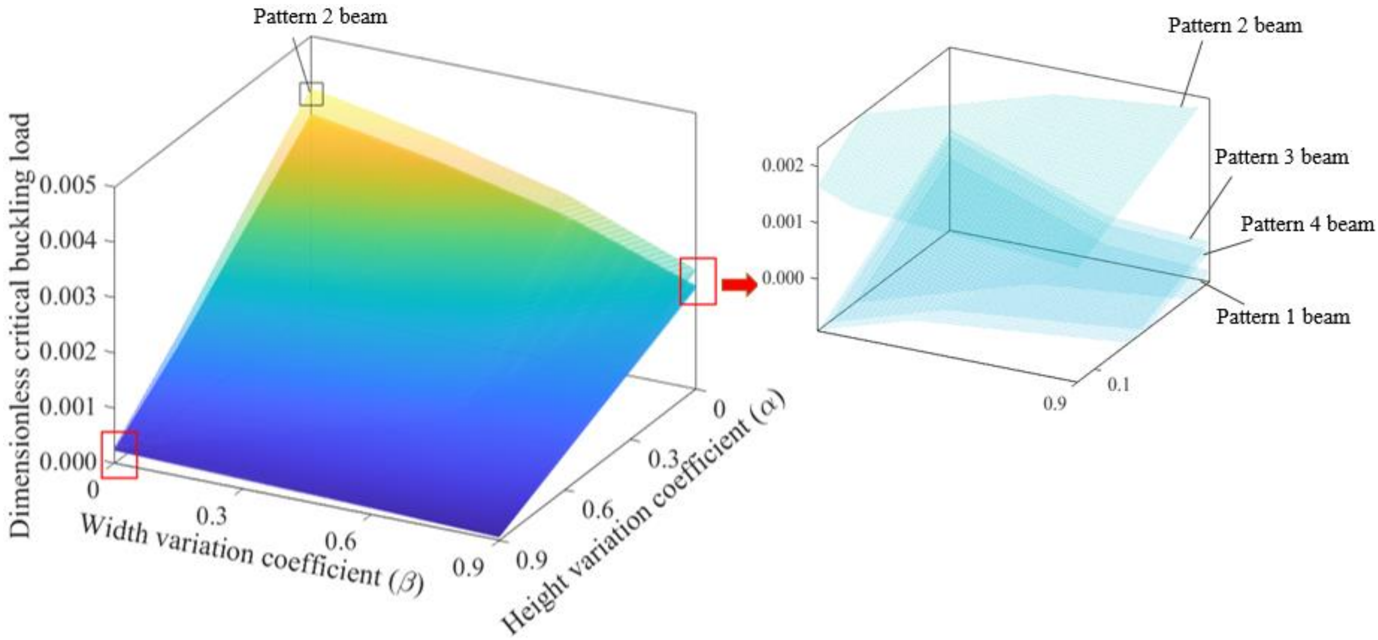

Fig. 8 Dimensionless critical buckling load of T1S1 beams with varying α and β. (N_0=0.5, L/h_0=20)

5.2.4 The influence of the dimensionless spring constants

The influence of the dimensionless spring constants is presented in this subsection. The curves of the dimensionless critical buckling load for T1S1 beams with changing the dimensionless spring constants under different taper ratio are shown in Fig. 9 below. The dimensionless axial spring constant (γ_A) is 10^8, and the dimensionless transverse spring constant (γ_T) is equal to the dimensionless rotational spring constant (γ_R) for the elastic boundary. Based on observation, an increase in the dimensionless spring constants leads to an increase in the dimensionless critical buckling load, and the critical buckling load converge to a particular value as the spring constants reach to a certain threshold. This is due to the fact that as the spring constants increase, the elastic support will tend to clamp support, where the dimensionless critical buckling load will converge and attain the maximum value. Furthermore, with decreasing τ, the change of critical buckling load of the beams before reaching the maximum value becomes more pronounced with an increase in spring constants for the reason that the greater stiffness of beams, the more sensitive they are to the alterations of boundary conditions. Equally important discovery is that the larger spring constants are required for the beams to attain the maximum buckling load which suggests that a higher spring stiffness is demanded to achieve the clamp support when τ decrease. Moreover, it is obvious that regardless of the taper ratio, the dimensionless critical buckling load of Pattern

2 beam approach to 0 when the spring constants are 0 which implies that the beam boundary condition is free-free support (F-F). This appearance displays that the buckling resistance of Pattern 2 beam under the free support boundary condition is smaller than that of other pattern beams.

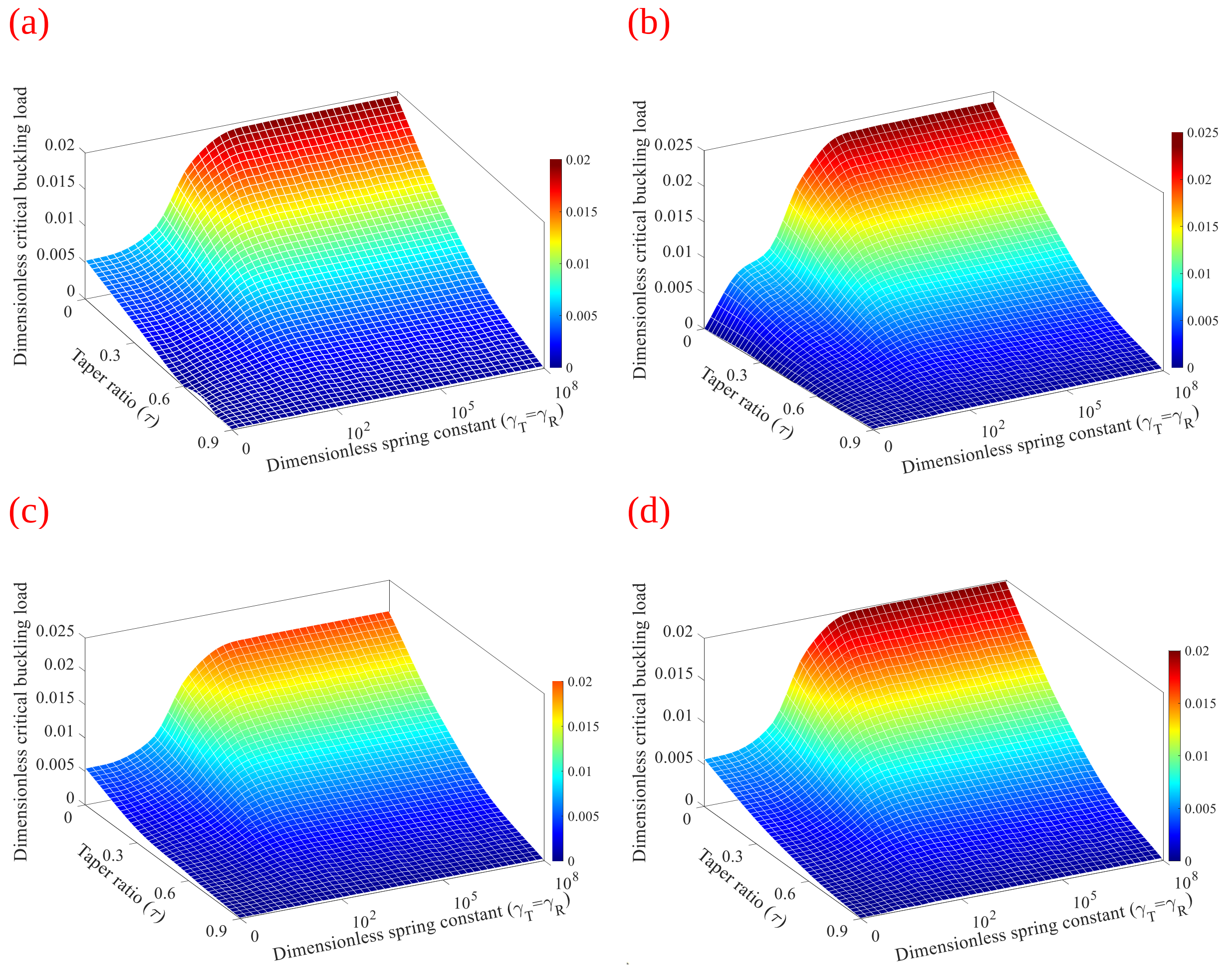

Fig. 9 Dimensionless critical buckling load of T1S1 beams with varying γ_T and γ_R under E-E boundary condition. (a) Pattern 1; (b) Pattern 2; (c) Pattern 3; (d) Pattern 4. (N_0=0.5, L/h_0=10)

5.2.5 The influence of the configuration of multi-span beams

This subsection investigates the buckling behavior of various models multi-span beams shown in Fig. 3, their cross-sectional dimensions and length value are related to the number of spans in this paper. Assuming that the number of span is N_{sp}, the total length of multi-span beams is L=1, the sub span length is L(x)= 1/ N_{sp}, and the largest width is 1/ N_{sp}. Table. 6 to Table. 8 express the value of dimensionless critical buckling load of multi-span beams for four patterns porosity distribution under different boundary conditions. Besides, bar charts for Pattern 2 porosity distribution beam shown in Fig. 10 (a), (b) and (c) are utilized to effectively illustrate the representative relationship between different configurations of multi-span beams. In terms of two-span beams and four-span beams, various configurations of beams have certain differences in the dimensionless critical buckling load. But in general, two-span and four-span beams with Type2 beam as the first span exhibit better buckling response than those with Type1 beam as the first span in various boundary conditions. Except for the subtle distinction in the buckling load under E-S-S-F boundary condition, T1S3 and T2S3 beams confirm similar buckling performance in other boundary conditions for the reason that those two types three-span beams have the same structural model. Based on the above conclusions, this subsection also takes Pattern 2 beam as an example to discuss the buckling load of multi-span beams with different number of spans and Type2 beam as the first span under different boundary conditions, as illustrated in Fig. 10 (d). For the convenience of analyzing the buckling behavior of different multi-span beams, the simply support between each span beam are ignored, and the boundary conditions of multi-span beams are simplified as E-E, E-F and F-F. Combining the height gap between each bar in the chart, it can obviously see that the more spans, the more likely that the beams will be unstable under E-E and F-F boundary conditions. However, the buckling load of four-span beams are significantly greater than that of two-span and three-span beams in the E-F boundary condition.

Table. 6 Dimensionless critical buckling load of the two-span beams for four patterns porosity distribution with varying boundary conditions ($\times 10^{-3}$). (S expressed in the boundary conditions represents the intermedia support is simply supported)

Boundary conditions	Taper ratio	Pattern 1	Pattern 2	Pattern 3	Pattern 4
T1S2 beams					
E-S-E	$\tau = 0$	3.235	3.843	3.322	3.293
	$\tau = 0.3$	1.699	2.016	1.743	1.729
	$\tau = 0.6$	0.610	0.726	0.626	0.621
	$\tau = 0.9$	0.041	0.050	0.042	0.042
T2S2 beams					
E-S-E	$\tau = 0$	3.235	3.843	3.322	3.293
	$\tau = 0.3$	1.929	2.298	1.982	1.964
	$\tau = 0.6$	0.754	0.920	0.777	0.770

	$\tau = 0.9$	0.061	0.076	0.063	0.063
T1S2 beams					
E-S-F	$\tau = 0$	0.354	0.434	0.364	0.373
	$\tau = 0.3$	0.127	0.156	0.131	0.134
	$\tau = 0.6$	0.025	0.031	0.026	0.027
	$\tau = 0.9$	0.001	0.001	0.001	0.001
T2S2 beams					
E-S-F	$\tau = 0$	0.354	0.434	0.364	0.373
	$\tau = 0.3$	0.247	0.303	0.254	0.259
	$\tau = 0.6$	0.132	0.163	0.136	0.138
	$\tau = 0.9$	0.016	0.020	0.017	0.017
T1S2 beams					
F-S-F	$\tau = 0$	0.603	0.746	0.621	0.002
	$\tau = 0.3$	0.220	0.000	0.227	0.001
	$\tau = 0.6$	0.044	0.000	0.046	0.000
	$\tau = 0.9$	0.001	0.000	0.001	0.001
T2S2 beams					
F-S-F	$\tau = 0$	0.603	0.746	0.621	0.002
	$\tau = 0.3$	0.000	0.481	0.400	0.001
	$\tau = 0.6$	0.000	0.227	0.189	0.000
	$\tau = 0.9$	0.000	0.000	0.018	0.000

Table. 7 Dimensionless critical buckling load of the three-span beams for four patterns porosity distribution with varying boundary conditions ($\times 10^{-3}$). (S expressed in the boundary conditions represents the intermedia support is simply supported)

Boundary conditions	Taper ratio	Pattern 1	Pattern 2	Pattern 3	Pattern 4
T1S3 beams					
E-S-S-E	$\tau = 0$	2.672	3.242	2.750	2.733
	$\tau = 0.3$	1.403	1.697	1.443	1.433
	$\tau = 0.6$	0.499	0.605	0.513	0.509

	$\tau = 0.9$	0.033	0.040	0.034	0.034
T2S3 beams					
E-S-S-E	$\tau = 0$	2.672	3.242	2.750	2.733
	$\tau = 0.3$	1.403	1.696	1.443	1.433
	$\tau = 0.6$	0.499	0.605	0.513	0.509
	$\tau = 0.9$	0.033	0.040	0.034	0.034
T1S3 beams					
E-S-S-F	$\tau = 0$	0.356	0.440	0.366	0.369
	$\tau = 0.3$	0.239	0.295	0.246	0.248
	$\tau = 0.6$	0.124	0.153	0.128	0.128
	$\tau = 0.9$	0.016	0.020	0.016	0.016
T2S3 beams					
E-S-S-F	$\tau = 0$	0.356	0.440	0.366	0.369
	$\tau = 0.3$	0.127	0.157	0.130	0.132
	$\tau = 0.6$	0.025	0.031	0.026	0.026
	$\tau = 0.9$	0.127	0.001	0.001	0.001
T1S3 beams					
F-S-S-F	$\tau = 0$	0.269	0.332	0.276	0.285
	$\tau = 0.3$	0.112	0.138	0.115	0.118
	$\tau = 0.6$	0.023	0.028	0.023	0.024
	$\tau = 0.9$	0.001	0.001	0.001	0.001
T2S3 beams					
F-S-S-F	$\tau = 0$	0.269	0.332	0.276	0.285
	$\tau = 0.3$	0.112	0.138	0.115	0.118
	$\tau = 0.6$	0.023	0.028	0.023	0.024
	$\tau = 0.9$	0.000	0.001	0.001	0.001

Table. 8 Dimensionless critical buckling load of the four-span beams for four patterns porosity distribution with varying boundary conditions ($\times 10^{-3}$). (S expressed in the boundary conditions represents the intermedia support is simply supported)

Boundary conditions	Taper ratio	Pattern 1	Pattern 2	Pattern 3	Pattern 4
T1S4 beams					
E-S-S-S-E	$\tau = 0$	1.129	1.442	1.154	1.128
	$\tau = 0.3$	0.167	0.060	0.051	0.183
	$\tau = 0.6$	0.086	0.101	0.089	0.087
	$\tau = 0.9$	0.013	0.017	0.014	0.020
T2S4 beams					
E-S-S-S-E	$\tau = 0$	1.129	1.442	1.154	1.128
	$\tau = 0.3$	0.601	0.846	0.934	0.648
	$\tau = 0.6$	0.251	0.307	0.257	0.253
	$\tau = 0.9$	0.017	0.020	0.017	0.017
T1S4 beams					
E-S-S-S-F	$\tau = 0$	0.961	1.143	0.978	0.949
	$\tau = 0.3$	0.100	0.496	0.022	0.217
	$\tau = 0.6$	0.006	0.009	0.008	0.007
	$\tau = 0.9$	0.019	0.000	0.019	0.000
T2S4 beams					
E-S-S-S-F	$\tau = 0$	0.961	1.143	0.978	0.949
	$\tau = 0.3$	0.462	0.640	0.626	0.491
	$\tau = 0.6$	0.188	0.240	0.195	0.187
	$\tau = 0.9$	0.017	0.019	0.017	0.017
T1S4 beams					
F-S-S-S-F	$\tau = 0$	0.190	0.186	0.171	0.230
	$\tau = 0.3$	0.083	0.142	0.153	0.061
	$\tau = 0.6$	0.017	0.021	0.020	0.019
	$\tau = 0.9$	0.000	0.000	0.001	0.000
T2S4 beams					
F-S-S-S-F	$\tau = 0$	0.190	0.186	0.171	0.230
	$\tau = 0.3$	0.136	0.020	0.309	0.128
	$\tau = 0.6$	0.017	0.021	0.005	0.018

$\tau = 0.9$	0.000	0.000	0.000	0.002

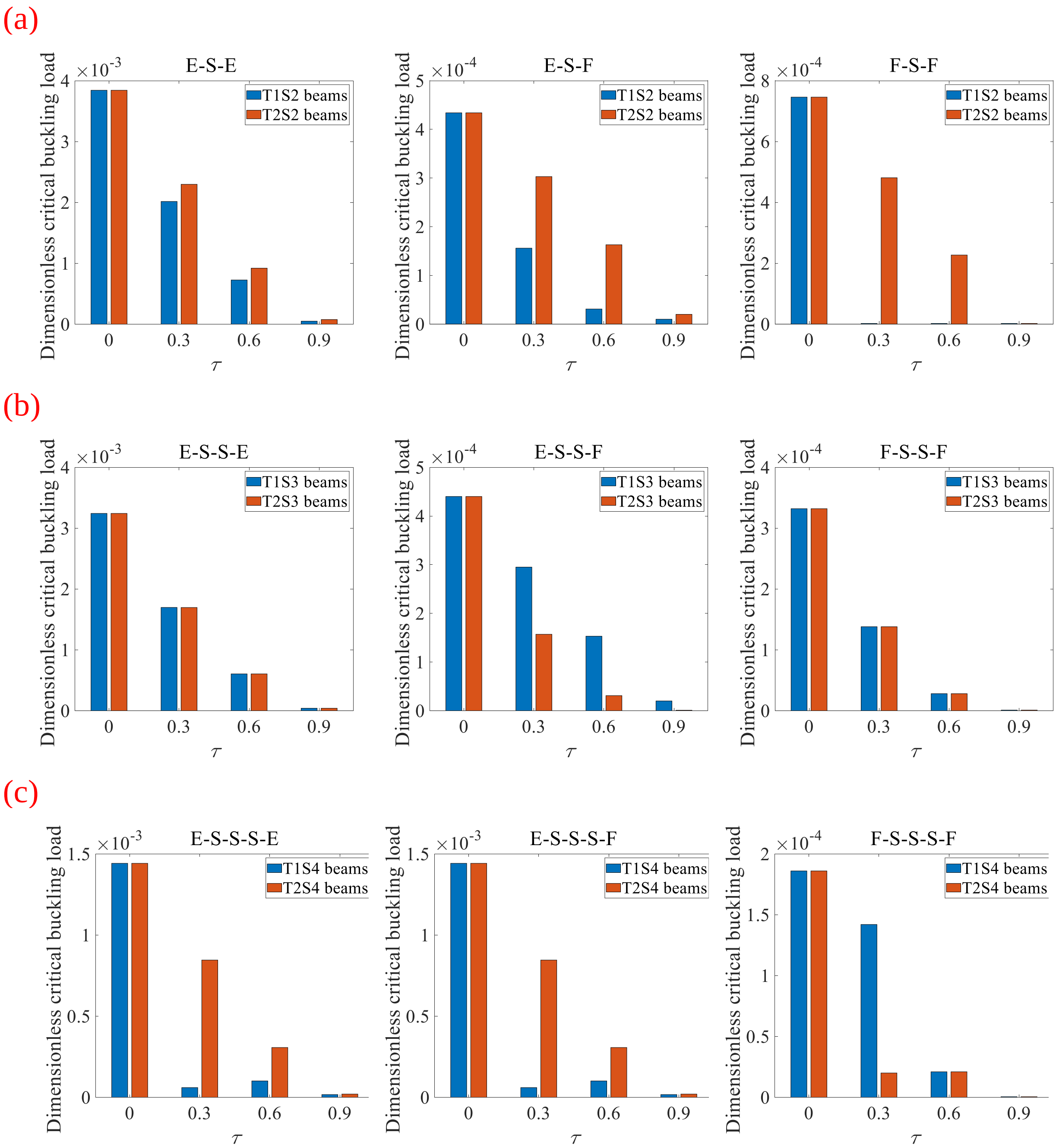

(d)

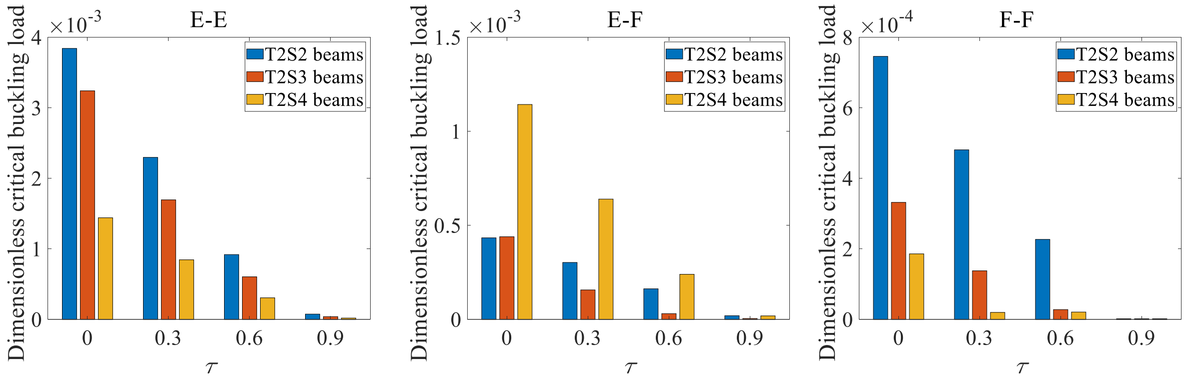

Fig. 10 Dimensionless critical buckling load of multi-span beams with Pattern 2 under different boundary conditions. (a) two-span beams; (b) three-span beams; (c) four-span beams; (d) T2S2, T2S3 and T2S4 beams.

6. Conclusions

The buckling behavior of FG 3D-GFs reinforced beams has been utilized by employing the DSC method for four patterns of reinforcement porosity distribution. The multi-span beams are formed by the diverse combinations of Type1 and Tyep2 beams, and spring restraints of various stiffness express the boundary conditions. Numerical investigation on the critical buckling load of such beams with different porosity coefficients, slenderness ratio, taper ratio, spring constants, and the configuration of multi-span beams. Based on the results discussed above, the following are the main contributions of this study:

According to the governing equation of buckling behavior, the increase of porosity coefficients decreases the critical buckling load, with the largest reduction load in Pattern 1 and Pattern 4 beams. Similarly, increasing the slenderness ratio reduces the critical buckling load for FG beams with four patterns of 3D-GFs reinforcement. Moreover, the larger the taper ratio (height variation, width variation), the smaller the beam stiffness, where the height change significantly affects the beam stiffness than that of width change. Overall, the critical buckling load is ranked in decreasing order for Pattern 2, Pattern 3, Pattern 4, and Pattern 1 beams.

Considering the actual application conditions, the smaller taper ratio is, the more sensitive the beam is to the spring stiffness for different constraints. Besides, while the boundary condition is free-free support, the beams with Pattern 2 porosity distribution exhibit the worst buckling response. Meanwhile, the selection of the type and the number of spans of the multi-span beams have a vital impact on the application of multi-span beams, for the reason that two-span and four-span beams with Type 2 beam as the first span exhibit superior buckling performance, while T1S3 and T2S3 beams present similar buckling response due to their same structural model. Furthermore, the more spans, the beams are more likely to buckle under E-E and F-F boundary conditions.

Acknowledgements

The work described in the present paper is fully funded by a research grant from the National Natural Science Foundation of China (52208151), Natural Science Foundation of Jiangsu Province (BK20210254), 2021 High-level Personnel Project Funding of Jiangsu Province (JSSCBS20210069) as well as the funding from UKRI-EPSRC (EP/Y023455/1). The authors are grateful for the financial support. The damage dataset supporting the conclusions of this article will be made available by the authors, without reservation.

Declaration of Competing Interest

The authors declare that they have no known competing financial interests or personal relationships that could have appeared to influence the work reported in this paper.

Data availability

Data will be made available on request.

Appendix A.

The *n*th derivative of the delta kernel of Dirichlet type:

$$\delta_{\sigma,\Delta}^{(n)}(x-x_k)=\left(\frac{d}{dx}\right)^n \delta_{\sigma,\Delta}(x-x_k) \tag{A.1}$$

The Regularized Shannon's kernel (RSK):

$$\delta_{\sigma,\Delta}(x-x_k)=\frac{\sin[(\pi/\Delta)/(x-x_k)]}{(\pi/\Delta)/(x-x_k)}\exp[-\frac{(x-x_k)^2}{2\sigma^2}] \tag{A.2}$$

The discretization parameter *r*:

$$r(\pi - B\Delta) > \sqrt{4.61\eta}\,,\quad M/r > \sqrt{4.61\eta} \tag{A.3}$$

where σ is the calculation parameter, Δ is the spacing between two calculation nodes.

Appendix B.

The function *f*(*x*) of DSC method:

$$f^{(1)}(x) \approx \sum_{k=-M}^{M} \delta_{\sigma,\Delta}^{(1)}(x - x_k) f(x_k) = \sum_{k=-M}^{M} A_k f(x_k) = \sum_{k=-M}^{M} A_k f_k \tag{B.1}$$

$$f^{(2)}(x) \approx \sum_{k=-M}^{M} \delta_{\sigma,\Delta}^{(2)}(x - x_k) f(x_k) = \sum_{k=-M}^{M} B_k f(x_k) = \sum_{k=-M}^{M} B_k f_k \tag{B.2}$$

where the symbols A_k and B_k represent the weighting coefficients associated with the first and second derivatives with respect to *x*, respectively.

The function *f*(*x*) based on Taylor series expansion:

$$f^{(1)}(x_i) \approx \sum_{k=0}^{N+1} \bar{A}_{ik} \bar{f}_k \qquad (i=0,\ 1,\ 2,\ \ldots,\ N-1) \tag{B.3}$$

$$f^{(2)}(x_i) \approx \sum_{k=0}^{N+1} \bar{B}_{ik} \bar{f}_k \qquad (i=0,\ 1,\ 2,\ \ldots,\ N-1) \tag{B.4}$$

where $\bar{A}_{ik}$ and $\bar{B}_{ik}$ are the weight coefficients for the 1st and 2nd derivatives respecting to *x* following the elimination of the degrees of freedom pertaining to fictitious points.

The governing equations of motion:

$$\begin{cases} A_{11} D2U + B_{11} D2\psi = 0 \\ \kappa_s A_{55}\left(D2W + D1\psi\right) = N_{x0} D2W \\ B_{11} D2U + D_{11} D2\psi - \kappa_s A_{55}\left(D1W + \psi\right) = 0 \end{cases} \tag{B.5}$$

where *D*1( ) and *D*2( ) represent the first and second derivatives of the three displacement components, and their expression are

$$\begin{bmatrix} D2U \\ D2W \\ D2\psi \end{bmatrix} = \begin{bmatrix} u^{(2)}(x_i) \\ w^{(2)}(x_i) \\ \varphi^{(2)}(x_i) \end{bmatrix} = \begin{bmatrix} \sum_{k=0}^{N+1} \bar{B}_{ij}\bar{u}_j \\ \sum_{k=0}^{N+1} \bar{B}_{ij}\bar{w}_j \\ \sum_{k=0}^{N+1} \bar{B}_{ij}\bar{\varphi}_j \end{bmatrix} \quad (i=0,\ 1,\ 2,\ \ldots,\ N\text{-}1) \tag{B.6}$$

$$\begin{bmatrix} D1W \\ D1\psi \end{bmatrix} = \begin{bmatrix} w^{(1)}(x_i) \\ \varphi^{(1)}(x_i) \end{bmatrix} = \begin{bmatrix} \sum_{k=0}^{N+1} \bar{A}_{ij}\bar{w}_j \\ \sum_{k=0}^{N+1} \bar{A}_{ij}\bar{\varphi}_j \end{bmatrix} \quad (i=0,\ 1,\ 2,\ \ldots,\ N\text{-}1) \tag{B.7}$$

Appendix C.

The boundary force equilibrium equations of the multi-span beams:

$$-F^0 + F_A^0 = 0,\ \left[F^{N-1}\right]_{①}^{-} - \left[F^0\right]_{②}^{+} + \bar{F}_A = 0,\ \ F^{N-1} + F_A^{N-1} = 0 \tag{C.1}$$

$$-V^0 + F_T^0 = 0,\ \left[V^{N-1}\right]_{①}^{-} - \left[V^0\right]_{②}^{+} + \bar{F}_T = 0,\ \ V^{N-1} + F_T^{N-1} = 0 \tag{C.2}$$

$$-M^0 + F_R^0 = 0,\ \left[M^{N-1}\right]_{①}^{-} - \left[M^0\right]_{②}^{+} + \bar{F}_R = 0,\ \ M^{N-1} + F_R^{N-1} = 0 \tag{C.3}$$

where F_A, F_T and F_R are the spring forces in the axial direction, transverse direction and rotational direction expressed by the spring coefficients κ_A, κ_T and κ_R. The spring forces expression are given as

$$\begin{bmatrix} F_A^0 \\ F_T^0 \\ F_R^0 \end{bmatrix} = \begin{bmatrix} \kappa_{LA}\bar{u}_0 \\ \kappa_{LT}\bar{w}_0 \\ \kappa_{LR}\bar{\varphi}_0 \end{bmatrix},\ \begin{bmatrix} \bar{F}_A \\ \bar{F}_T \\ \bar{F}_R \end{bmatrix} = \begin{bmatrix} \bar{\kappa}_A\bar{u} \\ \bar{\kappa}_T\bar{w} \\ \bar{\kappa}_R\bar{\varphi} \end{bmatrix},\ \begin{bmatrix} F_A^{N-1} \\ F_T^{N-1} \\ F_R^{N-1} \end{bmatrix} = \begin{bmatrix} \kappa_{RA}\bar{u}_{N-1} \\ \kappa_{RT}\bar{w}_{N-1} \\ \kappa_{RR}\bar{\varphi}_{N-1} \end{bmatrix} \tag{C.4}$$

where κ_{LA}, κ_{LT} and κ_{LR} are the spring coefficients corresponding to the elastic support located at the left end of two-span beam in the axial direction, transverse direction and rotational direction. $\bar{\kappa}_A$, $\bar{\kappa}_T$ and $\bar{\kappa}_R$ are the spring coefficients related to the intermediate elastic support. Similarity, κ_{RA}, κ_{RT} and κ_{RR} indicate the spring coefficients of the two-span beam right end elastic support. It's worth mentioning that the classical boundary conditions can be achieved by adjusting the spring coefficients. Besides, 0 and N-1 indicated by the superscript are the initial node and the tail node of each span beam, '–' combined with ① mean the end of the first span beam and the left side of the shared node, and '+' in conjunction with ② signify the beginning of the second span beam and the right side of the shared node.

Nine formulas to obtain the degrees of freedom at the common node:

$$\begin{cases} \left[A_{11}u^{(2)}\left(x_{N-1}\right)+B_{11}\varphi^{(2)}\left(x_{N-1}\right)\right]^{-}_{\textcircled{1}}+\left[A_{11}u^{(2)}\left(x_{0}\right)+B_{11}\varphi^{(2)}\left(x_{0}\right)\right]^{+}_{\textcircled{2}}=\left[\partial F/\partial x\right]^{-}_{\textcircled{1}}+\left[\partial F/\partial x\right]^{+}_{\textcircled{2}} \\ \left[A_{11}u^{(2)}\left(x_{N-1}\right)+B_{11}\varphi^{(2)}\left(x_{N-1}\right)\right]^{-}_{\textcircled{1}}-\left[A_{11}u^{(2)}\left(x_{0}\right)+B_{11}\varphi^{(2)}\left(x_{0}\right)\right]^{+}_{\textcircled{2}}=\left[\partial F/\partial x\right]^{-}_{\textcircled{1}}-\left[\partial F/\partial x\right]^{+}_{\textcircled{2}} \\ \left[\kappa_s A_{55}w^{(2)}\left(x_{N-1}\right)+\varphi^{(1)}\left(x_{N-1}\right)\right]^{-}_{\textcircled{1}}+\left[\kappa_s A_{55}w^{(2)}\left(x_{0}\right)+\varphi^{(1)}\left(x_{0}\right)\right]^{+}_{\textcircled{2}}=\left[\partial V/\partial x\right]^{-}_{\textcircled{1}}+\left[\partial V/\partial x\right]^{+}_{\textcircled{2}} \\ \left[\kappa_s A_{55}w^{(2)}\left(x_{N-1}\right)+\varphi^{(1)}\left(x_{N-1}\right)\right]^{-}_{\textcircled{1}}-\left[\kappa_s A_{55}w^{(2)}\left(x_{0}\right)+\varphi^{(1)}\left(x_{0}\right)\right]^{+}_{\textcircled{2}}=\left[\partial V/\partial x\right]^{-}_{\textcircled{1}}-\left[\partial V/\partial x\right]^{+}_{\textcircled{2}} \\ \quad \left[B_{11}u^{(2)}\left(x_{N-1}\right)+D_{11}\varphi^{(2)}\left(x_{N-1}\right)-\kappa_s A_{55}\left(w^{(1)}\left(x_{N-1}\right)+\varphi\left(x_{N-1}\right)\right)\right]^{-}_{\textcircled{1}} \\ \quad +\left[B_{11}u^{(2)}\left(x_{0}\right)+D_{11}\varphi^{(2)}\left(x_{0}\right)-\kappa_s A_{55}\left(w^{(1)}\left(x_{0}\right)+\varphi\left(x_{0}\right)\right)\right]^{+}_{\textcircled{2}}=\left[\partial M/\partial x\right]^{-}_{\textcircled{1}}+\left[\partial M/\partial x\right]^{+}_{\textcircled{2}} \\ \quad \left[B_{11}u^{(2)}\left(x_{N-1}\right)+D_{11}\varphi^{(2)}\left(x_{N-1}\right)-\kappa_s A_{55}\left(w^{(1)}\left(x_{N-1}\right)+\varphi\left(x_{N-1}\right)\right)\right]^{-}_{\textcircled{1}} \\ \quad -\left[B_{11}u^{(2)}\left(x_{0}\right)+D_{11}\varphi^{(2)}\left(x_{0}\right)-\kappa_s A_{55}\left(w^{(1)}\left(x_{0}\right)+\varphi\left(x_{0}\right)\right)\right]^{+}_{\textcircled{2}}=\left[\partial M/\partial x\right]^{-}_{\textcircled{1}}-\left[\partial M/\partial x\right]^{+}_{\textcircled{2}} \\ \quad \left[F^{N-1}\right]^{-}_{\textcircled{1}}-\left[F^{0}\right]^{+}_{\textcircled{2}}=\Delta F \\ \quad \left[V^{N-1}\right]^{-}_{\textcircled{1}}-\left[V^{0}\right]^{+}_{\textcircled{2}}=\Delta V \\ \quad \left[M^{N-1}\right]^{-}_{\textcircled{1}}-\left[M^{0}\right]^{+}_{\textcircled{2}}=\Delta M \end{cases} \tag{C.5}$$

where ΔF , ΔV and ΔM denote the external axial load, external shear load, and external bending moment exerted at the connection.

Appendix D.

The expression of the partitioned matrix

$$[\mathbf{K}]=\begin{bmatrix}[K_{aa}] & [K_{ab}]\\ [K_{ba}] & [K_{bb}]\end{bmatrix},\quad [\mathbf{V}]=\begin{bmatrix}[V_{aa}] & [V_{ab}]\\ [V_{ba}] & [V_{bb}]\end{bmatrix},\quad \{\mathbf{d}\}=\begin{Bmatrix}\{d_a\}\\ \{d_b\}\end{Bmatrix} \tag{D.1}$$

where $[K_{aa}]$ and $[K_{ab}]$ are the global DSC weighting coefficient matrices, $[K_{ba}]$ and $[K_{bb}]$ are the boundary conditions matrices, $\{d_a\}$ is the points in the interior domain, $\{d_b\}$ is the points at the boundary.

The expression of the rewritten partitioned matrix:

$$[\tilde{\mathbf{K}}]=[K_{aa}]-[K_{ab}][K_{bb}]^{-1}[K_{ba}],\quad [\tilde{\mathbf{V}}]=[V_{aa}]-[V_{ab}][V_{bb}]^{-1}[V_{ba}] \tag{D.2}$$

Appendix E.

The dimensionless critical buckling load and the dimensionless spring constant factors:

$$P_{cr}=\frac{N_{x0}}{A_{110}},\quad \begin{cases}\gamma_A=\kappa_A L(1-v^2)/E_{\max}h\\ \gamma_T=\kappa_T L(1-v^2)/E_{\max}h\\ \gamma_R=12\kappa_R L(1-v^2)/E_{\max}h^3\end{cases}\tag{E.1}$$

where A_{110} is the value of A_{11} for the pure 3D-GFs reinforcement beam.

References

[1] Naebe M, Shirvanimoghaddam K. Functionally graded materials: A review of fabrication and properties. Appl Mater Today 2016;5:223-45.

[2] Xu FX, Zhang X, Zhang H. A review on functionally graded structures and materials for energy absorption. Eng Struct 2018;171:309-25.

[3] Lee C, Wei XD, Kysar JW, Hone J. Measurement of the elastic properties and intrinsic strength of monolayer graphene. Science 2008;321:385-8.

[4] Ding H-X, Eltaher MA, She G-L. Nonlinear low-velocity impact of graphene platelets reinforced metal foams cylindrical shell: Effect of spinning motion and initial geometric imperfections. Aerosp Sci Technol 2023;140.

[5] Zhang Y-W, She G-L, Ding H-X. Nonlinear resonance of graphene platelets reinforced metal foams plates under axial motion with geometric imperfections. Eur J Mech A-Solid 2023;98.

[6] Idowu A, Boesl B, Agarwal A. 3D graphene foam-reinforced polymer composites - A review. Carbon 2018;135:52-71.

[7] Wang XB, Zhang YJ, Zhi CY, Wang X, Tang DM, Xu YB, et al. Three-dimensional strutted graphene grown by substrate-free sugar blowing for high-power-density supercapacitors. Nat Commun 2013;4.

[8] Li N, Zhang Q, Gao S, Song Q, Huang R, Wang L, et al. Three-dimensional graphene foam as a biocompatible and conductive scaffold for neural stem cells. Sci Rep 2013;3.

[9] Brownson DAC, Figueiredo LCS, Ji XB, Gomez-Mingot M, Iniesta J, Fatibello O, et al. Freestanding three-dimensional graphene foam gives rise to beneficial electrochemical signatures within non-aqueous media. J Mater Chem A 2013;1:5962-72.

[10] Choi BG, Yang M, Hong WH, Choi JW, Huh YS. 3D macroporous graphene frameworks for supercapacitors with high energy and power densities. Acs Nano 2012;6:4020-8.

[11] Zhu R, Liu XN, Hu GK, Sun CT, Huang GL. A chiral elastic metamaterial beam for broadband vibration suppression. J Sound Vib 2014;333:2759-73.

[12] Carrera E, Pagani A, Petrolo M, Zappino E. Recent developments on refined theories for beams with applications. Mech Eng Rev 2015;2:14-00298-14-.

[13] Zhu K, Chung J. Dynamic modeling and analysis of a spinning Rayleigh beam under deployment. Int J Mech Sci 2016;115-116:392-405.

[14] Sayyad AS, Ghugal YM. Bending, buckling and free vibration of laminated composite and sandwich beams: A critical review of literature. Compos Struct 2017;171:486-504.

[15] He C-H, Liu C, He J-H, Gepreel KA. Low frequency property of a fractal vibration model for a concrete beam. Fractals 2021;29.

[16] Salem T, Jiao P, Zaabar I, Li X, Zhu R, Lajnef N. Functionally graded materials beams subjected to bilateral constraints: Structural instability and material topology. Int J Mech Sci 2021;194.

[17] Nikolić A. Bending, buckling, and free vibration analysis of multi-span beams. Eng Today 2022.

[18] Thai H-T. A nonlocal beam theory for bending, buckling, and vibration of nanobeams. Int J Eng Sci 2012;52:56-64.

[19] Vo TP, Thai H-T. Vibration and buckling of composite beams using refined shear deformation theory. Int J Mech Sci 2012;62:67-76.

[20] Li XY, Wang XH, Chen YY, Tan Y, Cao HJ. Bending, buckling and free vibration of an axially loaded timoshenko beam with transition parameter: Direction of axial force. Int J Mech Sci 2020;176.

[21] Lanc D, Vo TP, Turkalj G, Lee J. Buckling analysis of thin-walled functionally graded sandwich box beams. Thin Wall Struct 2015;86:148-56.

[22] Nguyen TT, Thang PT, Lee J. Flexural-torsional stability of thin-walled functionally graded open-section beams. Thin Wall Struct 2017;110:88-96.

[23] Yang ZC, Wu D, Yang J, Lai SK, Lv JE, Liu AR, et al. Dynamic buckling of rotationally restrained FG porous arches reinforced with graphene nanoplatelets under a uniform step load. Thin Wall Struct 2021;166.

[24] Belarbi MO, Salami SJ, Garg A, Hirane H, Amine DA, Houari MSA. Finite element bending and buckling analysis of functionally graded carbon nanotubes-reinforced composite beam under arbitrary boundary conditions. Steel Compos Struct 2022;44:437-57.

[25] Lee J. Application of Chebyshev-tau method to the free vibration analysis of stepped beams. Int J of Mech Sci 2015;101-102:411-20.

[26] Zhao Z, Wen SR, Li FM. Vibration analysis of multi-span lattice sandwich beams using the assumed mode method. Compos Struct 2018;185:716-27.

[27] Jin YQ, Luo XW, Liu HX, Qiu BS, Chi HY. An accurate solution method for vibration

analysis of multi-span lattice sandwich beams under arbitrary boundary conditions. Thin Wall Struct 2022;175.

[28] Li YX, Gong J. Free and forced vibration analysis of general multiple beam systems. Int J Mech Sci 2022;235.

[29] Xie WC. Buckling mode localization in randomly disorderde multispan continuous beams. Aiaa J 1995;33:1142-9.

[30] Liu LX, Yang WY, Chai YY, Zhai GF. Vibration and thermal buckling analyses of multi-span composite lattice sandwich beams. Arch Appl Mech 2021;91:2601-16.

[31] Avetisyan A, Ghazaryan K, Marzocca P. Stability of a finite length multi-span beam resting on periodic rigid and elastic supports. Int J Solids Struct 2023;281.

[32] Heydari A, Shariati M. Buckling analysis of tapered BDFGM nano-beam under variable axial compression resting on elastic medium. Struct Eng Mech 2018;66:737-48.

[33] Pai PF, Huang L, Gopalakrishnamurthy SH, Chung JH. Identification and applications of boundary effects in beams. Int J Solids Struct 2004;41:3053-80.

[34] Butcher EA, Sevostianov I, Burton T. On the separation of internal and boundary damage from combined measurements of electrical conductivity and vibration frequencies. Int J Eng Sci 2008;46:968-75.

[35] Li W, Song ZW, Chai YB. Discrete singular convolution method for dynamic stability analysis of beams under periodic axial forces. J Eng Mech 2015;141.

[36] Tam MF, Yang ZC, Zhao SY, Zhang HN, Zhang YY, Yang J. Nonlinear bending of elastically restrained functionally graded graphene nanoplatelet reinforced beams with an open edge crack. Thin Wall Struct 2020;156.

[37] Raffo JL, Grossi RO. A study on mode shapes of beams with internal hinges and intermediate elastic restraints. Mecánica Compu 2012;31:2593-610.

[38] Zhang Y, Lu Y, Wang S, Liu X. Vibration and buckling of a double-beam system under compressive axial loading. J Sound Vib 2008;318:341-52.

[39] Ariaei A, Ziaei-Rad S, Malekzadeh M. Dynamic response of a multi-span Timoshenko beam with internal and external flexible constraints subject to a moving mass. Arch Appl Mech 2013;83:1257-72.

[40] Ghorbanpour-Arani AH, Abdollahian M, Ghorbanpour Arani A. Nonlinear dynamic analysis of temperature-dependent functionally graded magnetostrictive sandwich nanobeams using

different beam theories. J Braz Soc Mech Sci 2020;42.

[41] Zheng DY, Fan SC. Natural frequencies of a non-uniform beam with multiple cracks via modified fourier series. J Sound Vib 2001;242:701-17.

[42] Tsiatas GC. Nonlinear analysis of non-uniform beams on nonlinear elastic foundation. Acta Mech 2009;209:141-52.

[43] Lenci S, Clementi F, Mazzilli CEN. Simple formulas for the natural frequencies of non-uniform cables and beams. Int J Mech Sci 2013;77:155-63.

[44] Li Q. Buckling of multi-step non-uniform beams with elastically restrained boundary conditions. J Constr Steel Res 2001;57:753-77.

[45] Li Q. Buckling of an elastically restrained multi-step non-uniform beam with multiple cracks. Arch Appl Mech 2002;72:522-35.

[46] Rajasekaran S, Khaniki HB. Bending, buckling and vibration of small-scale tapered beams. Int J Eng Sci 2017;120:172-88.

[47] Chen D, Wang Y, Peng X, Zhou L. Dynamic buckling of axially functionally-graded beams with non-uniform cross-section under elastic compression stress wave. J Vib Shock 2017;36:27-32,73.

[48] Lin BC, Chen B, Zhu B, Li JA, Li YH. Dynamic stability analysis for rotating pre-twisted FG-CNTRC beams with geometric imperfections restrained by an elastic root in thermal environment. Thin Wall Struct 2021;164.

[49] Gao K, Huang Q, Kitipornchai S, Yang J. Nonlinear dynamic buckling of functionally graded porous beams. Mech Adv Mater Struc 2021;28:418-29.

[50] Ebrahimi F, Dashti S. Free vibration analysis of a rotating non-uniform functionally graded beam. Steel Compos Struct 2015;19:1279-98.

[51] Wei GW. Discrete singular convolution for the solution of the Fokker-Planck equation. J Chem Phys 1999;110:8930-42.

[52] Suming X. The discrete singular convolution algorithm-basic principle and applications [Master]: Nanjing University of Aeronautics and Astronautics 2012.

[53] Civalek Ö. Three-dimensional vibration, buckling and bending analyses of thick rectangular plates based on discrete singular convolution method. Int J Mech Sci 2007;49:752-65.

[54] Wei GW. Discrete singular convolution for beam analysis. Eng Struct 2001;23:1045-53.

[55] Wei GW. Vibration analysis by discrete singular convolution. J Sound Vib 2001;244:535-53.

[56] Wei GW, Zhao YB, Xiang Y. The determination of natural frequencies of rectangular plates with mixed boundary conditions by discrete singular convolution. Int J Mech Sci 2001;43:1731-46.

[57] Wei GW, Zhao YB, Xiang Y. Discrete singular convolution and its application to the analysis of plates with internal supports. Part 1: Theory and algorithm. Int J Numer Meth Eng 2002;55:913-46.

[58] Wei GW. A new algorithm for solving some mechanical problems. Comput Method Appl M 2001;190:2017-30.

[59] Wei GW, Zhao YB, Xiang Y. Discrete singular convolution and its application to the analysis of plates with internal supports. Part 1: Theory and algorithm. Int J Numer Meth Eng 2002;55:913-46.

[60] Bourihane O, Ed-Dinari A, Braikat B, Jamal M, Mohri F, Damil N. Stability analysis of thin-walled beams with open section subject to arbitrary loads. Thin Wall Struct 2016;105:156-71.

[61] Ni Z, Fan YC, Hang ZY, Zhu F, Wang Y, Feng C, et al. Damped vibration analysis of graphene nanoplatelet reinforced dielectric membrane using Taylor series expansion and differential quadrature methods. Thin Wall Struct 2023;184.

[62] Wang X, Yuan Z. Discrete singular convolution and Taylor series expansion method for free vibration analysis of beams and rectangular plates with free boundaries. Int J Mech Sci 2017;122:184-91.

[63] Lei YL, Gao K, Wang XW, Yang J. Dynamic behaviors of single- and multi-span functionally graded porous beams with flexible boundary constraints. Appl Math Model 2020;83:754-76.

[64] Qin Z, Jung GS, Kang MJ, Buehler MJ. The mechanics and design of a lightweight three-dimensional graphene assembly. Sci Adv 2017;3.

[65] Kitipornchai S, Chen D, Yang J. Free vibration and elastic buckling of functionally graded porous beams reinforced by graphene platelets. Mater Design 2017;116:656-65.

[66] Sayyad AS, Ghugal YM. Bending, Buckling and free vibration analysis of size-dependent nanoscale FG beams using refined models and Eringen's nonlocal theory. Int J Appl Mech 2020;12.

[67] Thai H-T, Vo TP. A nonlocal sinusoidal shear deformation beam theory with application to bending, buckling, and vibration of nanobeams. Int J Eng Sci 2012;54:58-66.